Methods in Molecular Biology 1607

Springer Protocols

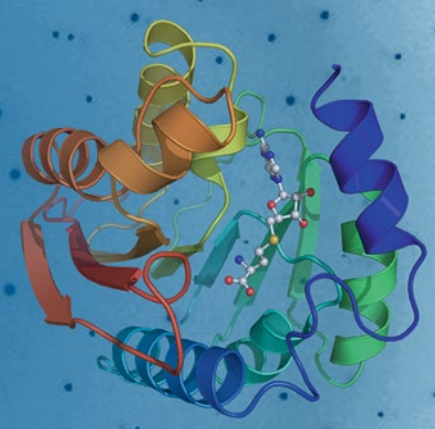

Alexander Wlodawer
Zbigniew Dauter
Mariusz Jaskolski *Editors*

Protein Crystallography

Methods and Protocols

Humana Press

Chapter 12

Structure Determination Using X-Ray Free-Electron Laser Pulses

Henry N. Chapman

Abstract

The intense X-ray pulses from free-electron lasers, of only femtoseconds duration, outrun most of the processes that lead to structural degradation in X-ray exposures of macromolecules. Using these sources it is therefore possible to increase the dose to macromolecular crystals by several orders of magnitude higher than usually tolerable in conventional measurements, allowing crystal size to be decreased dramatically in diffraction measurements and without the need to cool the sample. Such pulses lead to the eventual vaporization of the sample, which has required a measurement approach, called serial crystallography, of consolidating snapshot diffraction patterns of many individual crystals. This in turn has further separated the connection between dose and obtainable diffraction information, with the only requirement from a single pattern being that to give enough information to place it, in three-dimensional reciprocal space, in relation to other patterns. Millions of extremely weak patterns can be collected and combined in this way, requiring methods to rapidly replenish the sample into the beam while generating the lowest possible background. The method is suited to time-resolved measurements over timescales below 1 ps to several seconds, and opens new opportunities for phasing. Some straightforward considerations of achievable signal levels are discussed and compared with a wide variety of recent experiments carried out at XFEL, synchrotron, and even laboratory sources, to discuss the capabilities of these new approaches and give some perspectives on their further development.

Key words XFEL, Serial crystallography, Radiation damage, Coherent diffractive imaging, Phasing, Microcrystallography

1 Introduction

X-ray free-electron lasers (XFELs) [1] offer a disruptive new technology for macromolecular structure determination. These sources produce extremely intense X-ray pulses of femtosecond duration that provide two distinct advantages for the investigation of biological molecules and their complexes. The first is that the pulses, if produced with short enough duration, outrun most of the processes of radiation damage, allowing for exposures that are many orders of magnitude greater than possible with other sources such as synchrotron radiation facilities or X-ray tubes. This in turn

Alexander Wlodawer et al. (eds.), *Protein Crystallography: Methods and Protocols*, Methods in Molecular Biology, vol. 1607,
DOI 10.1007/978-1-4939-7000-1_12,

means that samples can be orders of magnitude smaller in volume than those required in conventional experiments, making possible measurements from samples too small or too weakly scattering to be feasible with conventional sources. Many protein systems produce numerous crystals of micrometer size or smaller before optimal crystallization conditions can be found that produce larger ones. By removing the need for large protein crystals, the crystallization bottleneck in the structure determination process can be alleviated. On the timescale of femtoseconds, below the periods of atomic vibrations, the concept of temperature loses its meaning and the sample under investigation is effectively frozen in time. There is thus no need to cryogenically cool samples, which can therefore be investigated under physiological conditions, giving access to conformational states or solvation conditions that may not be otherwise apparent. Electron densities of protein crystal structures obtained using XFEL pulses usually appear much better than counterparts elucidated using synchrotron sources even for the same crystallographic resolution, including better definition of side chains and disulfide bridges [2, 3] or metal binding sites [3].

There is a rather serious consequence of this approach of outrunning radiation damage in that the illuminated sample is completely vaporized by the pulse, at least at pulse fluences beyond 10^8 photons/μm^2. This means that only a single snapshot diffraction pattern can be obtained per object, and that the sample must be rapidly replenished to collect many thousands of patterns, one by one, ideally at the repetition rate of the XFEL. For crystalline samples this requirement results in an experimental design that is quite different from usual protein crystallography experiments where diffraction is collected as a crystal is rotated on a goniometer. Instead, the approach of "serial crystallography" is to record snapshot diffraction patterns one at a time, each from a fresh crystal that is usually delivered to the beam in a random and unknown orientation. Many tens of thousands or even millions of such patterns can be accrued in a time that depends on the pulse repetition rate and detector frame rate. Several different schemes for introducing and replenishing the sample to the beam are currently utilized in such experiments, discussed below and shown in Fig. 1, including high-speed liquid jets [4, 5], extruded pastes or gels [6–8], aerosol beams [9], or rapid scanning of samples mounted on or across solid supports [10–12]. For structure determination, the still snapshots of the diffraction pattern cannot be treated in isolation but must be oriented in three-dimensional reciprocal space (usually by indexing the observed Bragg peaks) and combined to obtain a full three-dimensional set of structure factors from the ensemble and, if the scattering is very weak, to build up adequate signal. The data processing strategy must also contend with the fact that the patterns are recorded from crystals of different shapes and sizes, with randomly fluctuating pulse intensities

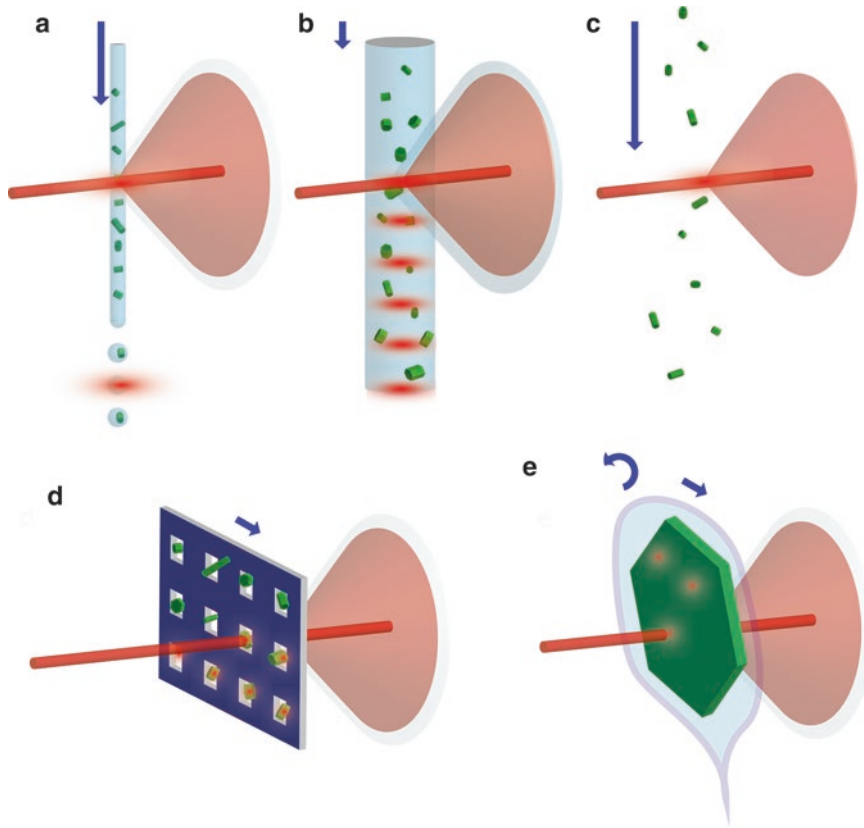

Fig. 1 Sample delivery options for serial crystallography. (**a**) Liquid micro-jet of 1–4 μm diameter gives low background and high speeds of many tens of meters per second. (**b**) Extrusion jets are slower, giving higher sample efficiency, but at the cost of higher background from about 50 μm thickness. (**c**) Aerosol injectors give the lowest background but also lowest efficiency and high speeds. (**a**–**c**) All can operate in vacuum. (**d**) Raster-scanned arrays can give 100% hit fractions for repetition rates of 120 Hz. (**e**) A large crystal mounted on a cryo-loop on a goniometer can be exposed in several places with known angular increments between pulses. Reprinted from [68]

and wavelengths (*see* Chapter 13 by White in this volume). In this sense, serial diffraction is not unlike powder diffraction (for crystalline samples) or wide-angle X-ray scattering (for single non-crystalline particles) measured one grain or particle at a time. Each Debye–Scherrer ring in a powder pattern is composed of individual reflections from different crystallites which can be integrated to average out any heterogeneities. Measuring the ensemble one crystalline grain at a time gives us the opportunity to interpret the structure factors in the three-dimensional space, merged as from an average "single" crystal, rather than collapsing data onto a less informative one-dimensional plot of intensity versus scattering angle [13], while still averaging over the ensemble. This realization leads to the possibility to decrease the specimen size even further from that attained by outrunning radiation damage. The total

required signal for structure determination can be distributed over many patterns, each from individual (but reproducible) objects. All that is needed from each of the patterns is enough information to be able to consolidate it with others in a common frame of reference in 3D reciprocal space. The rather daring culmination of this idea is single-molecule diffraction [14, 15], although there are many structural arrangements other than the extremes of single molecules and 3D crystals, such as 1D fibers, 2D crystals [16], and gases of aligned molecules [17], that can be addressed this way.

The second advantage of using X-ray FEL radiation is that the short duration of the pulse obviously enables measurements of time-varying structures, potentially with a very high temporal resolution. The evolution of structures at timescales below 1 ps have been followed in crystalline samples by synchronizing an optical "pump" pulse to arrive at the sample moments before the X-ray measurement pulse [18, 19]. The motions of the entire protein structure can be tracked in this way, following a photo-activated reaction such as the dissociation of a ligand from an active site [18] or an isomerization of a chromophore [19], with a time resolution given by the convolution of the durations of the optical and X-ray pulses and the uncertainty in the difference of their arrival times at the sample. The crystals that can be measured with XFEL pulses can be considerably smaller than the optical extinction depth of the pump light, meaning that the entire volume of the crystal can be uniformly photoexcited. Since a new sample is introduced into the beam for every X-ray pulse, irreversible reactions can be studied. It would be possible to witness the initial evolution of an explosive reaction, for example—the explosion induced by the X-ray interaction would be more violent in any case. Many experiments are carried out using slurries or suspensions of small crystals that flow across the X-ray beam in the form of a liquid jet that moves at speeds of several tens of meters per second, which can be illuminated at the X-ray interaction point or further upstream of the flow, depending on the time delay. The scheme of the flowing jet also enables fast mixing experiments where a ligand is brought into contact with a protein to follow the dynamics of their binding, for example. Here again the small crystal sizes offer improved experimental conditions since the diffusion times (which set the time resolution of such a mixing measurement) in micrometer-sized crystals can be substantially less than 1 ms [20].

2 Diffraction Before Destruction

A focused X-ray pulse from a free-electron laser is so intense that it vaporizes any material, turning it into plasma. Yet it is this extreme peak intensity (defined as the number of photons per unit area and time), a billion times higher than achievable from a synchrotron

radiation facility, that gives some reprieve from the effects of radiation damage that usually limit the X-ray exposure that a sample can tolerate and which otherwise require large well-diffracting crystals to overcome. This damage is unavoidable and occurs because tens of photons are absorbed in the sample for each photon that is scattered and contributes to the diffraction pattern. The photoexcited atoms emit photoelectrons which themselves carry enough energy to collisionally ionize hundreds of other atoms, leading eventually to heat generation, broken bonds, mobile radicals and solvated electrons that interact with reactive components of the molecules in the crystal, changing their structure [21]. Each photoionization imparts the energy of the photon to the sample, and the X-ray dose is measured by the total X-ray energy removed from the beam per unit mass (or number of atoms) in the sample, with SI units of Gray (1 Gy = 1 J/kg). For a given crystal size, the dose and the resulting degree of damage is thus proportional to the strength of the pattern recorded. While this unavoidable damage is a consequence of immutable atomic cross sections, it is possible to avoid many of the effects of this damage on the measured diffraction pattern by using a pulse that can "outrun" those effects [14]. In an exposure of a single XFEL pulse, any given photon interacts with atoms that could have only encountered any prior disturbance within a time less than the pulse duration, which may be 10–30 fs or less. Radicals certainly have no time to diffuse (even if created), and even if every single atom was ionized directly by a photon (which would occur in biological materials at a dose above ~50 GGy [22]), displacements of ions due to the strong Coulomb repulsion between them take some finite time to occur. The short XFEL pulse allows a dramatic increase in the strength of a diffraction pattern that can be recorded from a biological sample, albeit in a single shot. The acquisition of full three-dimensional structural information requires many serial measurements to be made on reproducible objects that are replenished on each X-ray pulse.

What is the physical limit to this concept of "diffraction before destruction"? The average scattering cross section of atoms in a protein is about 10^{-15} μm^2 for a photon energy of 8 keV [23], which means that 10^{15} photons/μm^2 would be required to scatter as many photons from a protein molecule as there are atoms in that molecule. The cross section for photoabsorption is about 30 times higher than the scattering cross section at this photon energy, yet there are not that many electrons in the atoms, so such processes will saturate. Emission of a photoelectron occurs essentially instantaneously on absorption of a photon, but there remains some time for the atom to relax after the ejection of one if its core-shell electrons. For the light elements, this primarily takes place by Auger decay, releasing yet another electron within a time of a few femtoseconds [24]. If another photoionization event takes place in an atom prior to Auger decay then the loss of both core electrons is described as a

"hollow atom" whose absorption cross section is significantly reduced, frustrating further ionization. In this way, it has been predicted that incident intensities of 10^{15} photons/μm^2 (and hence a dose of about 1 TGy) could give rise to about 0.1 scattered photons per atom, if delivered with a 1 fs pulse [24]. However, even during this time, atoms will be ionized by collisions with photoelectrons, which can be avoided with a pulse as short as 0.1 fs. Such a short X-ray pulse is still many wavelengths in length, enough to give rise to interpretable diffraction, but the generation of X-ray pulses of this intensity is beyond current capabilities. Below fluences of 10^{14} photons/μm^2 (100 GGy dose) and pulse durations below 100 fs the number of scattered photons per atom is predicted to be linearly proportional to fluence [24], as assumed in Fig. 2.

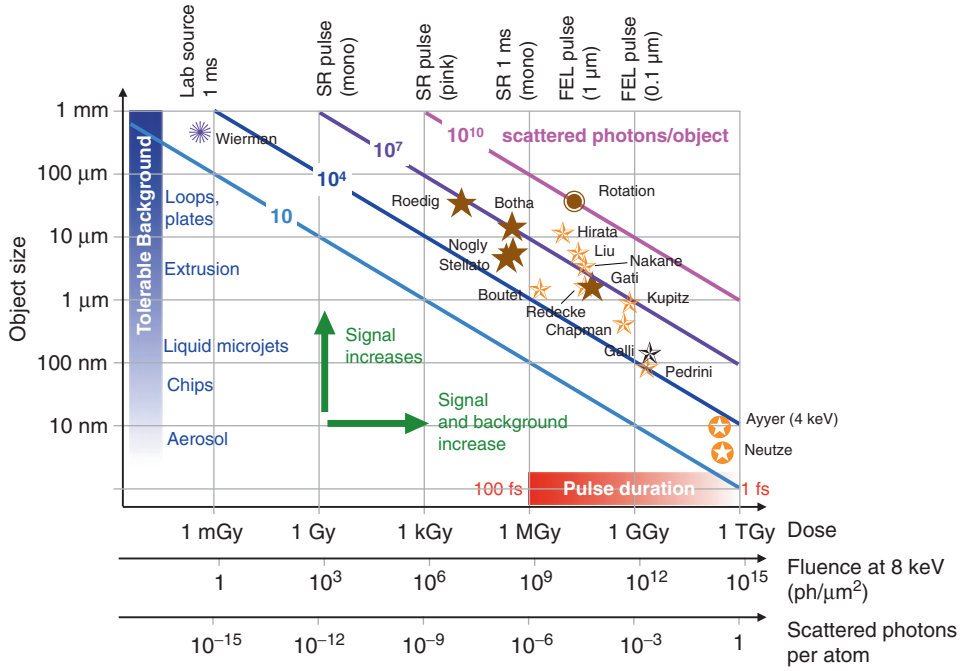

Fig. 2 A selection of serial crystallography experiments plotted on a log-log graph of crystal size versus dose. The dose is proportional to the number of X-ray interactions per atom and, for a given wavelength, the number of diffracted photons per atom, and provides a better means for comparison over different wavelengths than incident fluence. The crystal size is computed as the cube root of the illuminated volume. The total diffracted signal for a particular stoichiometry is proportional to the product of the number of diffracted photons per atom and object volume, shown as *solid lines*. *Orange* symbols correspond to XFEL experiments, *brown* to experiments at synchrotron radiation facilities, and *purple* illustrates an experiment using a laboratory source. For a given experiment, the background counts increase with X-ray fluence and hence the higher-fluence measurements from smaller crystals require delivery techniques that generate less background (described in *blue*). As fluence is increased in XFEL experiments, the pulse duration must be reduced, as indicated in *red*, requiring higher pulse powers. References are as follows: Wierman [42], Roedig [102], Stellato [103], Nogly [104], Botha [105], Boutet [106], Hirata [61], Liu [2], Nakane [55], Redecke [38], Gati [107], Chapman [73], Kupitz [108], Pedrini [109], Galli [47]. The data for the rotation series were extracted from [110]

The discussion here serves to provide a baseline to consider diffraction measurements made over a broad range of conditions, such as depicted in Fig. 2. A nanocrystal of, say, $10 \times 10 \times 10$ unit cells should yield a similar total diffraction signal as that of a single molecule at a dose that is 10^{-3} of 100 GGy (that is, at 100 MGy), for example, giving rise to 10^{-4} diffracted photons per atom, or perhaps about 1000–10,000 total diffracted photons depending on the size of the molecule. Whether such diffraction from a single molecule or crystal could be interpreted depends on the relative contribution to the scattering pattern due to background, which is difficult to reduce with such high-fluence incident beams. Thus, most serial crystallography experiments are carried out with larger micro-crystals at lower fluence, at doses of about 10–100 MGy, with a corresponding decrease in background. The dependence of structural change during the pulse depends both on the incident beam fluence (the dose) and also the pulse duration. Longer pulses give time both for a cascade of electron collisional ionization events to take place, and for nuclear motion. Each photoelectron of 8 keV energy has the potential to create over 300 additional ionizations, over a period of about 100 fs and thus can be drastically reduced with a pulse of 10 fs or even more so with 1 fs [25]. Nuclear motion is driven by Coulomb repulsion between ions as well as the electron heating, and was observed in early experiments at LCLS to develop to about 5 Å RMS displacement after the end of a 100 fs pulse delivering 3 GGy dose [26]. Surprisingly, Bragg peaks from protein crystals could still be observed when using such long pulses. The explanation for this was that peaks were formed in the early stages of the pulse, before disorder in atom positions stifled further contribution into Bragg peaks. Thus Bragg diffraction, which is dependent only on the periodic part of the structure, is regulated by the explosion. However, given that molecular structures are not homogeneous, and in particular heavier atoms have higher photoionization cross sections, it could be expected that such disorder does not progress uniformly throughout the molecule. Some recent experiments on ferredoxin crystals at doses of up to 30 GGy show the effects of using long (80 fs) pulses in which native Fe atoms (which have larger absorption cross sections and thus undergo more photoionization events) disturb their surroundings, with correlated displacements of atoms away from the Fe atoms [27]. Modeling indicates that pulse durations below 20 fs are required. Such pulse durations would not avert nonuniform photoionization, but this effect opens up the possibility for new methods in phasing by anomalous diffraction [28, 29]. In one scheme, the difference of data collected at low and high X-ray pulse fluences could identify the positions of heavier (more easily ionized) atoms [30].

These experiments and theoretical understanding show that for a given X-ray flux, a shorter pulse is always better. Thus the highest exposures required for the strongest patterns must be delivered

with pulses of high peak power (energy per unit time), focused down to submicrometer dimensions. A fluence of 10^{14} photons/μm^2 delivered in a pulse of 1 fs in a beam spot of FWHM of 0.1 μm, would require a source power of 10^{13} photons/fs, or a power of 10 TW for 8 keV photons (when accounting for the fact that beamlines cannot transport the entire XFEL output without loss). As yet, XFELs do not generate pulses of this power, but proposed schemes exist to exceed 10 TW [31]. Currently at the LCLS it is possible to deliver a pulse of about 10^{12} photons to a spot size of 0.2 μm with a pulse duration less than 20 fs, which should give rise to about 0.01 scattered photons per atom [28]. For a molecular complex like photosystem II with 72,000 atoms, this corresponds to almost 1000 photons per molecule. As seen in Subheading 3, this may be enough to provide interpretable diffraction. Defining a somewhat lower intensity regime, we can consider what dose could be tolerated for longer pulses of about 100 fs to several picoseconds. This is long enough for a fully developed electron cascade, but too short for transport of radicals [32]. Consider the case where every atom in the sample has been collisionally ionized by the end of the pulse, which implies that less than ~1% of atoms are photoionized (depending on the photon energy and if the system is large enough to trap all photoelectrons). Under this condition, most photons that interact with atoms will do so with neutral atoms; that is, with atoms that have not absorbed a photon nor been collisionally ionized. The probability of a fluorescence photon (for spectroscopy) being emitted by a perturbed atom, or an elastic scattering event (for diffraction) from a perturbed atom, will thus be small, given that the measurement is integrated over the pulse and the sample is initially neutral. The dose for this condition has been estimated at about 400 MGy for protein crystals measured with 100 fs pulses [22], compared with a tolerable dose of 30 MGy [21, 33] for cryogenically cooled samples measured with conventional sources and exposure times usually much longer than 1 ms.

Before closing this section on radiation damage, we consider some relevant points for conducting serial diffraction experiments at the much lower incident intensities of synchrotron sources since these are further discussed below. Radiation damage to protein crystals under such conditions has been extensively studied [34] although the ever-increasing brightness of these facilities, combined with beamline optics providing smaller X-ray spot sizes and improved detectors, opens up previously unexplored regimes of intensity and dose rate. The mean free path of high-energy photoelectrons in a protein crystal is on the order of 1 μm, giving crystals smaller than this size a higher dose tolerance, since many photoelectrons will deposit their energy (through the ensuing cascade of collisions) outside the crystal [35]. If the beam is bigger than the crystal then photoelectrons generated in any liquid or ice surrounding the crystal could feed into the crystal, reducing this advantage,

but if the beam is substantially smaller than the crystal then the energy can be deposited into a larger volume (of crystal or surrounding) than from which the diffraction originates. Note that for a given crystal thickness and number of incident photons, the integrated Bragg intensities are independent of the spot size, meaning that higher quality data should be obtainable with an X-ray beam focus smaller than the photoelectron mean free path. This is supported by some recent experiments at the ESRF [36]. These discussions bring into relief the exact definition of dose: which mass is the energy distributed over? Given that energy can flow out of the system by a variety of means and over a large range of timescales, a suitable definition (that we use in this chapter) is the energy lost by the X-ray beam over the mass that the beam interacts with. The degree of the subsequent damage, which may occur over a longer time or greater mass than the diffracting volume, is a separate and complex issue (*see* Chapter 20 by Garman in this volume).

3 Serial Crystallography

Destructive pulses demand a strategy of replenishing the sample on every X-ray pulse, measuring single-shot diffraction patterns at the rate of those delivered pulses. This serial approach is in contrast to the best practice in conventional crystallography, which is to sweep a wedge of reciprocal space populated by many fully integrated reflections, by rotating a single crystal (or acquiring several rotation series from several crystals), to obtain accurate estimates of structure factors. Instead, the snapshots collected in serial crystallography may consist entirely of Bragg peaks that are not located in the centers of their reflecting conditions, and the patterns may be rather noisy. (For a monochromatic parallel incident beam, the 2D snapshot diffraction pattern maps to a spherical surface of 3D reciprocal space called the Ewald sphere. The Ewald sphere need not cut through the center of the reciprocal lattice nodes, which for physical crystals have finite extensions.) These deficits are made up by collecting a large number of such patterns, building up the information in a fragmented, rather than systematic, way. This approach lessens the connection between dose, crystal size, and the total collected exposure, so that it is no longer necessary to heavily expose a single crystal or to be compelled to wring the last diffracted photon from a crystal that has already suffered significant radiation damage and photo-reduction. Even with small crystals measured using synchrotron radiation, the need to cryogenically cool samples can be avoided by limiting the exposure (amounting to a dose of less than 10 kGy, for example), giving only limited diffraction information, before measuring the next crystal. Of course, if a large enough crystal is available to enable the collection of complete and accurate data at low dose, then clearly a rotation series provides the best strategy to determine the static structure.

The comparison of serial crystallography to powder diffraction further makes it clear that it is not necessary that each crystal gives strong diffraction or is exposed to accumulate its full tolerable dose. A powder pattern may consist of fewer total scattered counts than the number of crystals in the powder sample and yet have high enough signal to be measured with high accuracy. The distinction between the two techniques is that in powder diffraction there is no requirement to treat crystals separately or to determine the orientation of each crystal, since the signal is an average over all crystal orientations (at the great cost of loss of information for structure determination). In powder diffraction, dose can be reduced arbitrarily by increasing the total ensemble size, avoiding absorption effects and background. Serial crystallography usually requires a certain minimum incident fluence (and hence a certain minimum dose), however, so that orientational information of each crystal can be discerned from its pattern to enable aggregation in a common frame of reference. The achieved signal levels in several experiments are plotted in Fig. 2 as a function of dose and crystal size. The required signal is much lower than for a rotation series where Bragg intensities must be determined with high accuracy (shown by the brown circle in Fig. 2). In most implementations of serial crystallography the requirement for each pattern is that the Bragg peaks can be accurately identified as such, and that they can be indexed in order to determine the lattice orientation. Signal levels usually exceed 10^4 scattered photons from the crystal and a much higher number of photons contributing to the background. After indexing, the intensities of the indexed peaks can then be combined with those from other patterns, after estimating corrections and relative scale factors, to build up estimates of structure factors at all observable reciprocal lattice points (*see* Chapter 13 by White in this volume). This common scenario is discussed below, but it is worth to consider how much further one can go. The knowledge of the lattice orientation of an individual pattern can be used to predict where even weaker (and perhaps undetectable) peaks reside in that pattern. The undetectable peaks have signal counts, I, much less than the noise in the background, σ. Just as in the case of cryo-electron microscopy, where individual images of macromolecules can barely be identified, let alone interpreted, the process of averaging a large number of noisy observations of the same Bragg peak that all have a signal-to-noise ratio (SRN) $I/\sigma \ll 1$ should finally reveal that peak and allow the estimation of the structure factor at that point in reciprocal space. As yet, this approach has not been fully exploited at XFEL sources, primarily because even submicrometer crystals are often large enough to give detectable Bragg peaks at high resolution, and there is usually not enough beamtime available (due to limited pulse repetition rates) for experimenters to keep acquiring data that are not immediately perceivable. Nevertheless, there are plenty of systems waiting to be measured, including proteins crystallized in vivo [37–39] and natural crystals [40].

But what happens if the patterns are too weak to discern any signal at all from noise, let alone discover the orientation of the crystal? If summed together, the powder pattern would eventually emerge from enough patterns. Using ideas of "cryptotomography" developed for the case of weak single-molecule diffraction, it is indeed possible to aggregate the data in 3D reciprocal space even with signals of only a few hundred total counts per pattern (i.e., less than 0.001 photon per pixel) [41, 42]. In particular, an expectation-maximization scheme in the form of the expand–maximize–compress (EMC) algorithm [43] iteratively generates a 3D volume of diffraction intensities from noisy patterns, ideally collected with not more than a single particle or crystal contributing to a pattern—that is, with no multiple hits. During this iterative process, the current estimate of the 3D intensities is used to extract Ewald slices that would be observed at particular crystal orientations. Each noisy pattern is compared with every extracted slice to determine the probability that it is a noisy manifestation of the extracted pattern, and then the 3D volume is updated by placing the measured patterns into that volume according to the probabilities. As this converges, the merged 3D diffraction volume becomes consistent with all of the measured patterns. So far, a proof-of-principle demonstration has been made using sets of sparse diffraction patterns collected with a laboratory source [41, 42] and convergence could be reached with about 200 photons per pattern (*see* purple star in Fig. 2). At these low counts, enough patterns are required in total to eventually populate almost 10^9 voxels of reciprocal space with several photons per voxel. In the study of Wierman et al. [42], this was achieved with 8.8 million recorded diffraction patterns, which were collected from one crystal in this case, to a resolution of 1.5 Å. If it had been carried out on 8.8 million individual crystals, the dose would have been less than 1 mGy (0.001 Gy) (as graphed in Fig. 2), instead of the total accumulated dose of about 3 kGy. It is interesting to scale this to the 500 GGy doses that are tolerable using short enough XFEL pulses, whereby one could reduce the crystal volume by a factor of 10^{14}, which essentially gives a single molecule. That is, it should be feasible to carry out single molecule diffraction in a regime of about 200 scattered photons per molecule, which may suffer from about 4000 ionizations per molecule when delivered with pulses longer than atomic relaxation times. It should be noted that the EMC algorithm or related methods of manifold embedding [44], do not distinguish or index Bragg peaks, but aggregate the full diffraction volume consisting of Bragg peaks, diffuse scattering, and more. Thus, while Bragg peaks are very useful for providing the lattice orientation at high signal levels (*see* Chapter 13 by White in this volume), it should still be possible to carry out serial diffraction with non-crystalline or semi-crystalline reproducible objects.

We thus see, as summarized in Fig. 2, that serial crystallography spans a wide range of exposures and doses, covering many

orders of magnitude, and ranging from the extreme case of almost as many scattered photons as atoms in the sample, to that of conventional crystallography of less than a single scattered photon per 10 or so molecules. Signal strengths range over about four orders of magnitude, depending on detector capabilities. The signals from small crystals are compensated with more intense pulses, but the background signal increases in direct proportion to incident flux, so the goal for sample delivery systems for these weakly scattering objects is to deliver them to the beam with as little extraneous material in the beam as possible (*see* Subheading 4, below). The role of background can be quite dramatic. When background dominates, halving it increases the SNR by a factor of two, requiring only $1/\sqrt{2}$ as many patterns to be collected, or having the same effect as doubling the volume of the crystal. Here we assume that the background is due to X-ray photons (obeying photon counting statistics) rather than electronic noise of the detector, or any other stray signal that would be measured when the X-ray beam is off. The overall signal-to-noise level of the merged diffraction intensities is ultimately limited by the number of patterns acquired: averaging noisy patterns is an exercise in the law of diminishing returns, depending on the square root of the number of patterns collected [45]. An example of the signal strength of diffraction of natural granulovirus particles illustrates these dependences. These virus particles consist of a crystalline shell of polyhedrin protein with a narrow size distribution and about 9000 unit cells per crystal for a crystalline volume of 0.01 μm^3 [46, 47]. Experiments carried out at the CXI instrument [48] of LCLS using a liquid micro-jet of about 3 μm diameter delivered a water suspension of granulovirus particles across the X-ray beam of 1 μm focus with 10^{12} photons per pulse and 7.9 keV photon energy [47], imparting a dose of up to 1.3 GGy (depicted in Fig. 2 as a black star). Diffraction patterns were recorded on a CS-PAD detector [49], and consisted of the diffuse background scatter from the liquid jet, as well as Bragg peaks from the polyhedrin crystal shell whenever a particle was in the focus at the arrival time of the pulse. At a resolution of 2 Å, the liquid background was about 10 photons per pixel, far in excess of the total counts in all Bragg peaks. Although Bragg peaks at this resolution could be observed occasionally, a total of 120,000 indexed patterns were needed to reach a SNR of 1, on average, in this resolution shell. As discussed above, the SNR increases with the square root of the number of patterns, and linearly with the crystal size. Since both the signal and background increase with fluence (or dose) the SNR increases with the square root of fluence (or dose), giving the empirical relationship of achievable SNR with liquid-jet background of

$$\mathrm{SNR}_{2\text{Å}} = \frac{1}{B + 0.1/\sqrt{2}} \sqrt{\frac{N_{\mathrm{patt}}}{120{,}000}} \frac{V_C}{0.01\mu\mathrm{m}^3} \sqrt{\frac{\mathrm{Dose}}{1.3\mathrm{GGy}}} \qquad (1)$$

where N_{patt} is the number of patterns and V_C is the volume of the crystal (assuming a similar unit cell volume as granulovirus, which is $(10\ \text{nm})^3$). The factor B gives the background counts per pixel relative to that generated by a 3 μm diameter liquid jet, and the factor of $0.1/\sqrt{2}$ approximates the effect of reducing the background to zero from 10 photons per pixel, although it should be noted that background counts depend on pixel size and binning. The number of patterns required to reach a given SNR at 2 Å resolution is therefore given by

$$N_{\text{patt}} = 1.2\times10^5\left(B+0.1/\sqrt{2}\right)^2 \text{SNR}_{2\text{Å}}^2\left(\frac{0.01\mu\text{m}^3}{V_C}\right)^2\frac{1.3\text{GGy}}{\text{Dose}} \quad (2)$$

Reducing the background by a factor of 10, equivalent to increasing the crystal volume by a factor of 10, would reduce the required number of patterns by a factor of about 100. Many crystals measured at XFELs have a volume of about 1 μm^3 or more, equivalent to 100 times more unit cells than granulovirus, requiring only 12 patterns to reach SNR = 1 (or 1200 patterns to reach a more desirable SNR = 10). That is, Bragg peaks of such crystals (if not disordered) can readily be observed at the LCLS, even with background from a 3 μm diameter jet. However, consider reducing the dose to just 1.3 kGy, a million times lower than in this example. For crystals of about 1 μm^3, that would require about 12 million patterns to be collected just to discern peaks above noise, or 120,000 patterns if crystals were delivered to the beam with a reduced background of a single count per pixel. At 8 keV photon energy, for an average protein, a dose of 1.3 kGy would be delivered with 10^6 photons/μm^2, which could easily be achieved using an undulator at a synchrotron source in a single bunch and without a monochromator (pink beam). Such bunches are typically 100 ps long, allowing time-resolved serial crystallography measurements at this resolution. Certainly at 1 kGy dose, radiation damage would be low, and some further advantage over radiation damage may be gained by outrunning radiolysis processes that take place on the nanosecond timescale [32]. Novel laboratory-based sources that are under development may provide similar numbers of photons in pulses of 0.1 fs duration [50].

Equation (2) shows that the total time for a serial crystallography measurement (of a static structure or for a particular condition or time-point in a series of measurements) depends on the average brightness of the source, which is to say the time required to conduct the experiment will be shorter if more patterns are collected per second. Interestingly, the dose, proportional to the peak X-ray fluence, can be offset by collecting more patterns, so that the total scattered counts in the experiment remains constant (proportional to the dose times the number of crystals or patterns). This holds at least to the point that there are enough scattered photons per pulse

to merge data in three dimensions, which might only be possible with the strongest possible pulses from XFELs, as seen in Fig. 2. The dead-time of the detector must be taken into account, and high repetition-rate sources can only be fully utilized if a detector is available that matches the repetition rate. Thus, while the highest-brightness synchrotron sources may exceed the average brightness of an XFEL operating at 120 Hz, experiments will take longer at the synchrotron without a detector operating at MHz frame rates. Here, the detectors must be integrating, not counting, devices. Even with the extremely sparse patterns that can be analysed with the EMC algorithm, signals may exceed a single count per pixel [42], and only integrating detectors could collect such signals. One of the highest frame-rate detectors currently under development is the AGIPD [51], capable of reading 3520 frames per second, in bursts separated by only 220 ns corresponding to the pulse pattern of the European XFEL, and as such this combination would provide the highest experiment brightness for serial crystallography. The future upgrade of the LCLS will likewise increase the repetition rates. With such source and detector combinations, measurements that take 10 h today at 120 Hz frame rate (such as low SNR measurement of 0.01 μm^3 crystals) will be completed in 20 min. Full datasets using crystals larger than 1 μm^3 could be acquired in tens of seconds.

Presently, most room-temperature serial crystallography experiments are carried out with crystals large enough to give detectable peaks at near the highest resolution of the final merged dataset. In these cases, the requirement on the number of patterns is to completely populate 3D reciprocal space with measurements and to average over fluctuations of the beam fluence and variations in crystal shape, size, and quality. The volume of reciprocal space that needs to be measured depends on the symmetry of the crystal. Symmetry operations of the diffraction intensities (or Patterson symmetry) are applied to each pattern, reducing the required number of measurements by the number of unique operations. (Some space groups cannot be unambiguously indexed based on the locations of the reciprocal lattice peaks alone—in this case the intensities must be compared to avoid creating a twinned dataset ([52] also *see* Chapter 13 by White in this volume).) In some cases fewer than 6000 indexed patterns could be used to obtain good estimates of structure factors [53]. 60,000 patterns were enough to produce high enough accuracy for phasing by single-wavelength anomalous diffraction [54] at LCLS using crystals of lysozyme in complex with a gadolinium (Gd) containing compound. The crystal volumes were smaller than 2 μm^3 and the dose was less than 30 MGy. Nakane et al. [55] required 150,000 indexed patterns from <1000 μm^3 crystals (with an illuminated crystal volume of about 20 μm^3, delivered in a grease matrix) and a dose of about 50 MGy to carry out native sulfur SAD phasing at 1.77 Å

wavelength (7 keV photon energy), an impressive feat of reaching the necessary low convergence errors. Some valuable lessons on how to obtain higher accuracies are given by Nass et al. [56]. As described in detail in Chapter 13 by White in this volume, metrics such as R-split can be used to monitor the precision of intensities determined from an ensemble of crystals measured serially. The R-split metric estimates the precision of the full dataset by comparing intensities derived from two random halves of the dataset (Nakane et al. achieved R-split =3.1% over the resolution range of 40–2.1 Å).

In general, crystal diffraction patterns are recorded with no more than a single crystal per shot, so that all Bragg peaks belong to a single reciprocal lattice. Methods for indexing multiple lattices have been developed [57–59], however, which allow a better experiment efficiency with the possibility to index more crystals than patterns. As the number of lattices per shot increases, so does the prevalence of overlapping or near-overlapping peaks, and the gain in efficiency is only obtained for a few crystals per shot. But when diffraction intensities other than Bragg peaks are to be used for analysis, such as the continuous diffraction from a disordered crystal (*see* below), then there must not be more than a single crystal per pattern. At XFELs the intrinsic bandwidth for SASE radiation is about 0.1%, and patterns are essentially treated as monochromatic. In fact, a broader bandwidth of up to about 4% is thought to provide better peak integration requiring fewer patterns (the volume of reciprocal space spanned by Ewald spheres of the wavelength range exceeds Bragg widths, especially at higher resolutions) [60]. Somewhat paradoxically, reducing the wavelength jitter by "seeding" the FEL generation processes does not improve convergence. At synchrotron radiation facilities with a suitable undulator, it would be possible to increase beam fluences more than 100-fold by eliminating the monochromator or by using a multilayer monochromator of a few percent bandwidth, enabling exposures in microseconds or even with single bunches (~100 ps exposures). However, broader-bandwidth Laue diffraction patterns are more difficult to index in an automated fashion than monochromatic patterns.

A substantial reduction in the required number of patterns can be achieved if it is possible to acquire multiple patterns from the same crystal in more than one orientation. This could be the case with a crystal large enough, so that multiple (destructive) exposures are acquired with a spacing larger than the distance the X-ray damage is able to travel within the crystal [61, 62], or with several extremely low-dose pulses measured at a synchrotron, for example. Since the damage propagation distance is much larger at room temperature than at cryogenic temperatures (and may extend over the entire crystal [3]), such experiments are best carried out with cryo-cooled samples [3, 61]. In both cases, the crystals must be

mounted in such a way that they can be rotated by a known amount between shots, increasing the complexity of the experiment. Such methods are a step towards the rotation series and the additional dependent measurements allow better estimation of parameters such as peak profiles and partialities, which in turn give more accurate estimates of the structure factors. In some cases it is possible to reject outlier patterns based on the results of indexing the Bragg peaks, which may or may not improve the final dataset [63]. It should be possible to separate distinct phases of materials in the beam that have different unit cell dimensions [64], or perhaps to carry out a cluster analysis based on the intensities or unit cell dimensions [65].

4 Sample Delivery Methods

There are almost as many methods to rapidly deliver protein crystals and small particles to the beam as there are groups carrying out serial diffraction experiments; such is the vigor and diversity of this young developing field. Some of these methods have been described in reviews [66–68] and they can be grouped into methods of continuously or repetitively flowing samples across the X-ray beam, or rastering through the beam of a two-dimensional matrix in which specimens are mounted or embedded, referred to, respectively, as "jetting" or "fixed targets," as illustrated in Fig. 1. As is obvious from the discussion above, serial diffraction measurements are as much about acquiring diffraction as they are about reducing background. As emphasized by Gruner and Lattman [69], there are many sources of background in conventional crystallography experiments and thus the common practices of mounting crystals and using protecting foils to prevent crystal dehydration, for example, must be modified or abandoned when crystals approach volumes of 1 μm^3. Sample supports and foils, surrounding amorphous ice, and air present a scattering cross section (integrated over the path of the X-ray beam) that may surpass that of a small crystal by many orders of magnitude (i.e., along the beam, there are more atoms of these objects than in the crystal) and thus they contribute many orders of magnitude more photons on the detector than the Bragg diffraction of the crystal. The concentration of crystal diffraction into Bragg peaks enables this signal to be detected even when more photons contribute to the diffuse background. This ratio of total signal photons to background is independent of the X-ray fluence, so precautions are universally needed. The microdiffraction beamlines at XFELs were designed for experiments to be carried out in vacuum, with samples held on thin membranes or delivered as an aerosol jet [70–72]. The first serial crystallography experiments at LCLS [73] were carried out using a liquid jet of several micrometers diameter of a suspension of submicrometer

crystals in their mother liquor. The thinness of the jet, and the fact that it could be sustained in the vacuum environment, were achieved using a gas-focusing nozzle which was one of the enabling inventions for the method [4, 5, 74].

Besides not generating too much background scatter, the delivery method should ideally not consume too much sample and should be able to replenish a new sample to the beam on each shot (possibly just before photoactivation), with the possibility of mixing or some other method of initiating a reaction. The properties of the delivery device therefore depend strongly on the repetition rate of the source, which spans 30 Hz at SACLA, 120 Hz at LCLS, to 4.5 MHz at the European XFEL (in bursts). For a flowing sample, efficiency can be parameterized by the "hit fraction," or the proportion of pulses that generate diffraction from a particle or crystal, sometimes referred to as the "hit rate." For short femtosecond pulses this can be approximated as $H = fA/(vw)$ for f particles per second injected at a velocity v as a stream of width w moving in a direction perpendicular to an X-ray beam of cross section A [75]. At any instant of time (such as when the X-ray pulse arrives) the areal density of particles or crystals as seen by the X-ray beam is $f/(vw)$. For a given consumption f, the density and hence the hit fraction are increased by slowing down the particles, which however must be travelling at a high enough speed so that the sample (and any expanding volume of destruction) clears the beam by the next pulse [76]. In this regard, in-air or in-vacuum extrusion injectors that flow crystals embedded in lipidic cubic phase [6], grease [7], or gel [8] provide speeds of several mm/s that are well matched to repetition rates of 30–120 Hz. Depositing the sample onto a moving tape (in air) also gives similar speeds [77]. The extruded pastes or moving tape are usually quite thick, however, giving rise to background counts that are many times higher than achievable with gas-focused liquid jets. Such micrometer-diameter gas-focused jets run at speeds of about 50 m/s, suitable for the MHz rates expected at the European XFEL and LCLS II. Recent developments of jetting two fluids concentrically allow for fast mixing prior to exposure [78–80] in a narrow gas-focused jet. Mixing times depend on diffusion across boundaries of liquids under laminar flow, but can be less than 1 ms, providing a temporal resolution on this order. The time delay can be continuously varied in a telescopic design or moving the nozzle position relative to the beam [79]. Faster mixing could be induced by more complicated flow-folding schemes, as used in microfluidic experiments [81].

For the mixing jet, one can also choose the sheath liquid based on its fluid properties that define the jet behaviour, such as viscosity and surface tension, giving a very reliable and stable sample delivery method [80], which may be appropriate for rapid structure determination at a dedicated station. Using the AGIPD detector, capable of reading 3520 patterns per second, 10^6 frames could

be recorded in less than 5 min at high repetition rate FELs, putting greater premium on reliability of jets and the ability to automatically change sample [67]. Even at the lower pulse rates, where sample consumption per pattern is much higher, liquid jets provide a convenient method to deliver samples in liquid form and at room temperature with reasonably low background, in vacuum, or ambient atmosphere. Elongated objects become aligned along their long axis by the nonuniform fluid velocity profile across the nozzle capillary, and they tend to retain this alignment in the jet. This has a benefit for fiber diffraction, and may enable the serial diffraction methods to obtain 3D structure factors from single-fiber patterns. For most 3D crystals, however, flow alignment can lead to a missing cone of measurements in reciprocal space, requiring the ability to tilt the jet relative to the X-ray beam direction.

The lowest possible background is achieved by aerosolizing the sample and entraining it with a low-pressure gas into a beam using an aerodynamic lens. This device consists of a series of concentric apertures in a larger-diameter tube. Laminar flow of the gas through the restrictions briefly concentrates the streamlines, but the particles cannot exactly follow these lines due to their momentum and instead tend to fly to the center of the flow [82]. Aerodynamic lenses have been used successfully for single-particle diffraction experiments at FLASH [9] and LCLS [83] and are under improvement and optimization to decrease the stream width w to below 10 μm [84]. In principle, this method should be suitable for injecting small crystals, as long as the residence in the aerosol does not dehydrate them. Particle speeds are on the order of 10–50 m/s. Simpler convergent nozzles have produced jet sizes smaller than 2 μm travelling faster than 200 m/s [75]. Experiments are underway to use optical forces to further concentrate such beams [85].

Raster-scanning a structure supporting many samples can give near 100% hit fractions with very little consumption of material and minimal background. Achieving all these conditions at once calls for a careful experimental design that depends on particle or crystal size, and placement of the sample in air or vacuum. Low background requires as thin support structure as possible, such as graphene or silicon nitride, as well as ensuring that the wings of the focused X-ray beam do not interact with the supporting frame (using low-scatter clean-up slits or aperture). If crystals are large enough they can be caught in open holes in a silicon chip [12] by using a clever method of pipetting a liquid suspension onto the chip and blotting from the rear. This wicks away most liquid, for low background. When the holes are arranged in a regular array, the chip can be rapidly scanned so that a fresh sample position is probed on each shot. With a spacing between the windows of ~50 μm, scan speeds of 20 mm/s allow measurements at 120 Hz [86] plus some overhead for reversing the scan direction. Unless

cryogenically cooled, these chips must be used in a humid atmosphere to prevent sample dehydration, which requires other precautions to minimize air scatter. It may be possible to sandwich the sample between graphene layers [87] to prevent dehydration in a vacuum environment. As with liquid jets, supporting surfaces might give rise to preferred orientation of crystals, which can be managed by the ability to tilt the chip. For serial diffraction at a low repetition-rate XFEL or synchrotron radiation source, these "fixed target" methods give optimum efficiencies and highest quality diffraction, although they present greater challenges for time-resolved measurements than the flowing methods, especially for irreversible reactions, where it must be ensured that only sample at one position on the chip is activated at a time.

5 Diffractive Imaging and Crystallography

The use of XFEL pulses has opened the way to structure determination not only for crystallites that are smaller than required by conventional means, but also for single non-periodic particles, two-dimensional crystals [16], fibers, and oriented molecules in the gas phase [17]. Diffraction measurements from micrometer-sized 3D crystals or smaller has also opened up several new possibilities to experimentally phase the diffraction patterns (that is, obtain phases without the use of a structural model), such as using measurable intensities between Bragg peaks that occur due to the finite extent of the crystal [88, 89], or using continuous diffraction that occurs due to deviation of the crystal structure from a perfect periodicity [90]. These ideas emerged primarily from investigations of diffraction of single (or non-periodic) objects and while that field of coherent diffractive imaging is very closely related to crystallography [91], it is worth making a brief digression to establish the core concepts in a common language.

The wavelength of X-rays is short enough to resolve atoms in a molecule. This means that the scattered waves from two neighboring atoms, illuminated coherently, can interfere at the detector to give a diffraction pattern consisting of fringes, first understood (at much longer wavelengths) in the famous Young's double-slit experiment. A molecule of more than two atoms will consist of many such pairs, each producing a fringe pattern that contributes to the overall diffraction and which encodes the spacing between the pair of atoms and direction between them. This composite fringe pattern, termed the diffraction pattern, is proportional to the square modulus of the Fourier transform of the electron density (the molecular transform). When inverse-Fourier-transformed, the diffraction pattern reveals a map, called the autocorrelation function, of the distribution of all the atom pairs in the object. By the wonderful reciprocity between real space and diffraction space, points in

the diffraction pattern correspond to single spatial frequencies (that is, fringes of electron density) in the object. A single snapshot of the diffraction pattern is two dimensional, so only a 2D selection of spatial frequencies of the three dimensional structure is recorded in a single snapshot pattern, on the surface of the Ewald sphere. Even though a single pattern contains depth information (due to the Ewald sphere curvature), full structural information requires patterns measured in many directions to fill out 3D space (which, in the scheme of diffraction before destruction, must arise from a supply of reproducible objects). From such measurements, a 3D image of the molecule's electron density can be synthesized by Fourier analysis, but to go beyond the 3D map of interatomic vectors between pairs of atoms to the actual map of the positions of those atoms, requires assigning phases to the measured diffraction intensities, which in turn assigns positions to the spatial frequencies that together generate the electron density image.

The scattering strengths of such single molecules are exceedingly weak, as seen in Fig. 2. Macromolecular structures are primarily obtained using a different strategy, in which the diffraction pattern is amplified by virtue of the arrangement of molecules in a periodic lattice of a crystal. To the degree that the molecules are identical in structure and orientation, each molecule in a crystal gives rise to the same diffracted wavefield, but originating from a different place in the lattice on which the relative phase of each wavefield depends. There are so many of these waves, diffracting from so many molecules in the crystal, that they mostly cancel out (for each wave there is likely to be another with opposite phase) except in those quite sparse directions that correspond to Bragg angles. These are the directions where every wave arrives at the detector after travelling from the source via the sample by exactly an integer multiple of the wavelength and thus constructively interferes with all others. The arrangement of Bragg peaks follows the Fourier transform of the crystal lattice, known as the reciprocal lattice. The constructive interference of the diffracted wavefields in the Bragg peaks gives a huge "coherency gain" [92], amplifying the strength of the single-molecule diffraction pattern by the number of molecules in the crystal, which can give a strong enough diffraction pattern within limited tolerable dose limits [33]. Unfortunately the sparsity of the Bragg peaks comes at a high cost in the ability to assign the phases needed to reconstruct the structure. By being able to measure the diffraction only at the discrete points of the reciprocal lattice rather than to observe the continuous molecular transform, the information content of the diffraction pattern is significantly reduced [93]. This information loss usually prevents the possibility to derive the phases from the intensities alone, unless extremely high resolution data is available (for the application of direct methods and algorithms such as charge flipping [94]). This so-called "phase problem" is the familiar state of affairs in

crystallography, requiring additional measurements such as multiple wavelength anomalous diffraction or isomorphous replacement to provide the needed missing information.

The continuous diffraction from a single non-periodic compact object does not suffer from the phase problem since there are generally more independent measurements in the diffraction intensities than needed to describe the object. The greatest distance between any pair of atoms in the object are those at opposite extremes of the object; these give the largest extent of the autocorrelation map. Since this map is just another representation of the diffraction data (obtained directly from the measured intensities by Fourier transformation) the number of independent measurements is equal to the number of independent points in the autocorrelation map. This itself has a much larger non-zero volume than the original object (the volume of all possible connections between atoms is larger than the actual distribution of atoms). The volume of the autocorrelation map of a spherically shaped molecule is eight times that of the object itself. Accounting for the centrosymmetry of the autocorrelation map, this still gives a constraint ratio [95] of four, i.e., fourfold surplus of the measured information content over what is needed to describe the object. This overdetermination factor depends on the shape of the object (and of its autocorrelation function) but not the resolution—that is, atomic resolution is not required. A successful approach to determine the phases is to use one of a class of algorithms that iteratively constrains the solution to be consistent with the measured diffraction and a priori information about the object's structure [96]. This additional information need not be very detailed, and may simply be that the object fits within a certain rectangular box that is smaller than the extent of the autocorrelation function [97]; that the electron density is positive; or that the histogram of electron densities follows a certain profile, common to related proteins.

For crystals, the number of independent Bragg intensities is usually smaller than what is needed to describe the object, unless atomic resolution is reached where the number of measurements comfortably exceeds the number of parameters needed to describe the atoms (i.e., their positions and amplitudes of vibrations) (*see* Chapter 22 by Jaskolski in this volume). At the usual resolutions obtained with protein crystals, an ambiguity arises because of the crystal periodicity. The autocorrelation map of the crystal repeats with the same periodicity as the crystal lattice, and so the unique volume is restricted to at most one half the volume of the unit cell (due to centrosymmetry). It is not possible to distinguish points in the correlation map as arising from the intramolecular (within the same molecule) or intermolecular context (between neighboring molecules). If there is no non-crystallographic symmetry and if the object fills the volume of the unit cell, then the measurements would only account for half of the information needed to describe

the molecule (at whatever resolution the diffraction extended to). This deficiency of information has long been recognized, and the earliest (unsuccessful) attempts of phasing protein crystal diffraction by Bragg, Perutz, and others used crystals of various states of dehydration, and thus different unit cell dimensions, to obtain measurements of the molecular transform at a higher density than possible from a single crystal [98]. When the solvent content exceeds 50% of the crystal volume, the information obtainable from the Bragg peaks should be higher than that of the unknown structure, allowing iterative phasing [91, 99].

A recent method that merges the approaches of crystallography and coherent diffractive imaging utilizes the continuous diffraction from crystals exhibiting translational disorder. Disorder of any kind in a crystal is a bane to the formation of Bragg peaks, which only form when there are correlations over many unit cells. If a molecule is displaced by a vector $\vec{\sigma}$ from its ideal position in the crystal lattice then the diffracted wavefield from that molecule is modulated by a phase ramp $\exp\left(-2\pi i\vec{\sigma}\cdot\vec{q}\right)$. Here the magnitude of the wave-vector transfer $\vec{q}$ is equal to $2\sin\theta/\lambda$ for a scattering angle 2θ and wavelength λ. At a Bragg peak corresponding to a particular resolution length $d = 1/q$, the wavefield of the displaced molecule will combine with those of others with a phase error of $2\pi\sigma/d$ if that displacement is in the direction corresponding to the Bragg peak. For example, a displacement of 1.5 Å would cause destructive interference (a phase shift of π) at a Bragg peak corresponding to 3 Å resolution. Small random displacements of all molecules in the crystal with a mean square displacement of $<\sigma^2>$ will lead to random phases for scattering angles at high enough resolution. Due to that randomness, for every phase shift there is likely to be an opposite phase shift, with the result that the constructive interference that gives rise to the formation of Bragg peaks will not occur. Instead, the diffracted wavefields of each molecule will sum incoherently, giving rise to the continuous diffraction pattern of a single molecule, multiplied by the number of molecules. At low resolutions ($d \gg \sigma$) the phase errors from the displacements will be small, and in that case the constructive interference of Bragg peaks will still occur, and there will be little or no continuous diffraction. In general, the Bragg intensities will be modulated by the well-known Debye–Waller factor, $\exp(-4\pi^2\sigma^2q^2)$ whereas the continuous diffraction will arise contrariwise with q as $1 - \exp(-4\pi^2\sigma^2q^2)$. The Bragg intensities are reduced by a factor of $1/e = 0.368$ at a resolution of $d = 2\pi\sigma$, and an RMS displacement of 1.5 Å would reduce the Bragg intensities by this amount at 9 Å resolution. The effects of the translational arrangement of identical objects on their diffraction patterns are illustrated in Fig. 3.

There are two important implications of translational disorder in a crystal. One is that the continuous diffraction of a translationally disordered crystal may extend to resolutions far beyond Bragg

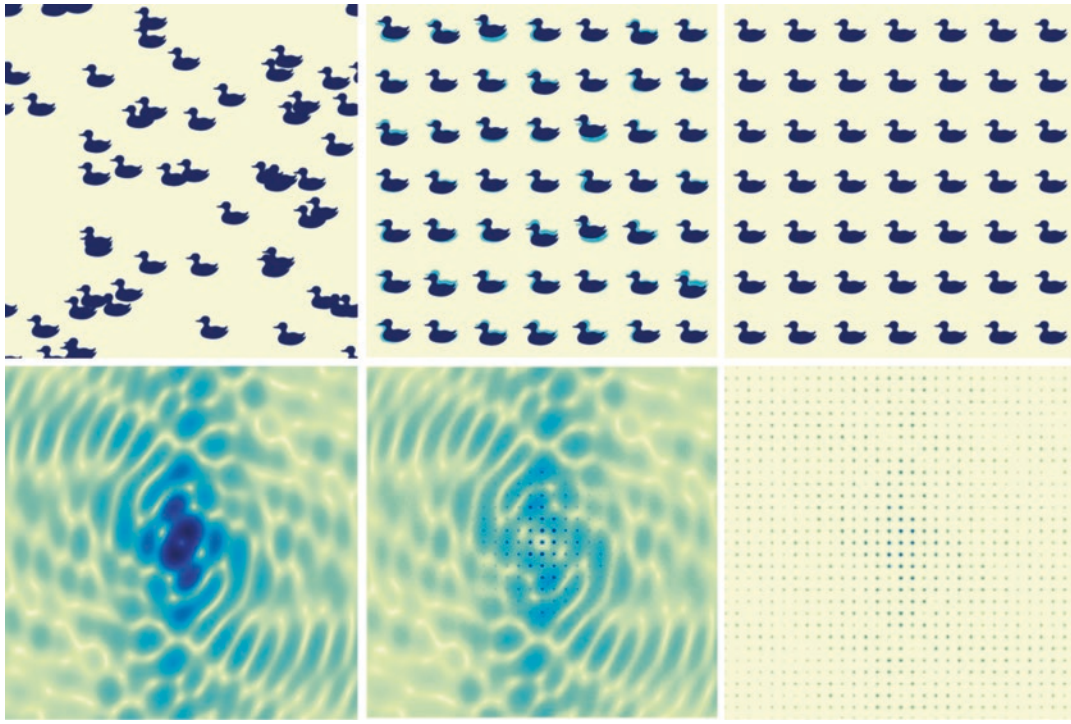

Fig. 3 Diffraction from an ensemble of similarly oriented objects depends on correlations between their positions. (**a**) A random arrangement of objects gives rise to the incoherent sum of the continuous diffraction pattern of each object (that is, *N* times the strength of the diffraction of a single object for *N* illuminated objects). (**b**) A crystal with a degree of translational disorder consists of Bragg peaks formed from the coherent sum of diffraction from all objects, modulated by a Debye–Waller factor that describes the suppression of Bragg peaks at resolutions greater than the disorder length divided by 2π. At those resolutions the incoherent sum of single-object diffraction occurs. (**c**) A perfect crystal produces solely the coherent sum of diffraction from the periodic array of scatterers

peaks—the resolution of useful information for structure determination is not necessarily limited by the extent (resolution) of the Bragg peaks. The second is that the continuous diffraction may be overdetermined by a significant factor, allowing iterative phasing methods to be used to obtain a 3D image of the molecule, without the need for a structural model [41]. The method was recently demonstrated on microcrystals of photosystem II which gave measurable Bragg peaks to a resolution of about 4.5 Å (Fig. 4). Continuous diffraction was observed to a resolution of 3.5 Å, limited by the detector extent and the number of patterns recorded. Several tests confirmed the origin of the continuous diffraction as the incoherent sum of the molecular diffraction from photosystem II dimers: the autocorrelation map computed directly from the continuous intensities was of finite extent with a boundary of the correct width and shape as corresponding to photosystem II molecules; the distribution of the intensities of the continuous

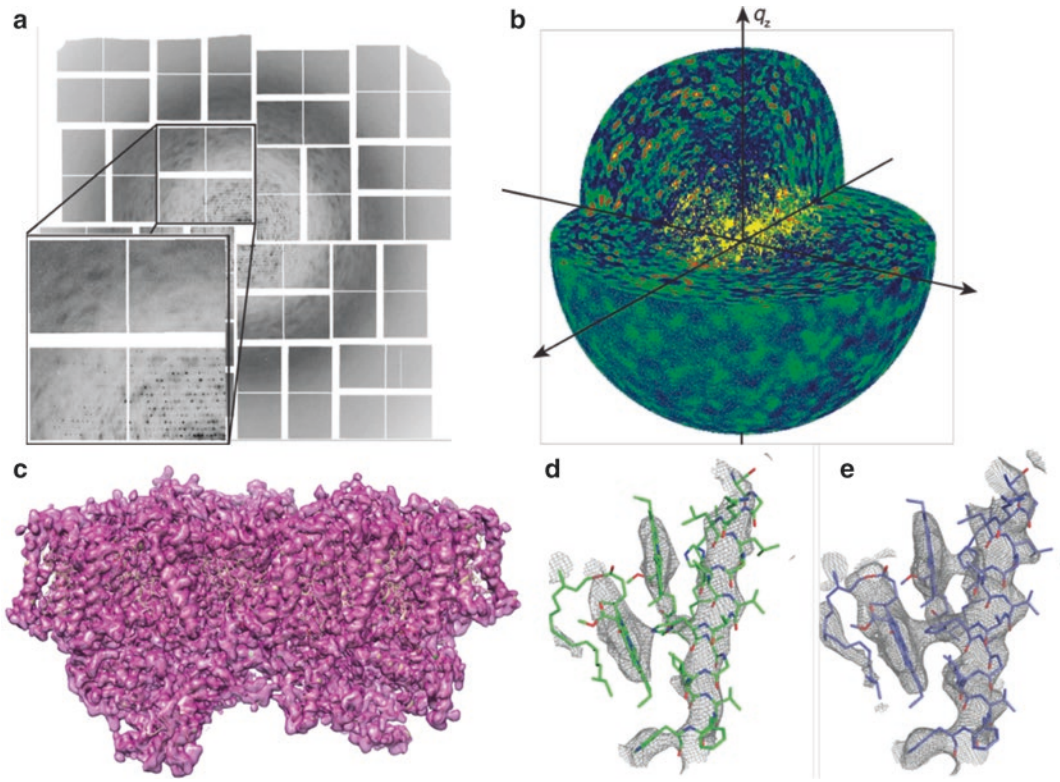

Fig. 4 Weak continuous diffraction (**a**) was observed in individual snapshot diffraction patterns recorded from photosystem II crystals at the LCLS [90]. When 2885 patterns were merged in a common frame of reference (defined by the indexed lattice) in 3D reciprocal space, the signal to noise of the continuous diffraction markedly improved, and extended significantly beyond the Bragg peaks (**b**). (**c**) The continuous diffraction could be phased using an iterative phasing algorithm to obtain a 3D image of the electron density of the photosystem II dimer. A detail of two chlorophylls of the dimer shows the improvement obtained from performing a structural refinement using the Bragg data only (to a resolution of 4.5 Å) (**d**) as compared with using together the Bragg and continuous diffraction (to a resolution of 3.5 Å) (**e**). Reprinted from [90]

diffraction followed Wilson statistics; and the diffraction could be phased by using a fixed support volume created by blurring out an initial electron density map obtained by refining a model using the Bragg intensities. The 3D image obtained by the continuous-transform phasing showed much clearer definition of structural elements such as α helices, even though the phasing algorithm had no knowledge of such structures (and the support, blurred to 8.9 Å resolution, showed no indication of these structures).

Translational disorder has not generally been expected in macromolecular crystals, although studies have been made on continuous diffraction from crystals of systems that undergo conformational dynamics [100]. It is common experience that many protein crystals only give Bragg diffraction to limited resolutions, and it is not unreasonable that the most dominant modes of disorder in a

crystal with high solvent content (and few crystal contacts) would be rigid-body translations and rotations of the biological structure, followed by internal displacements. Such may be the case for membrane proteins and other large complexes which form very delicate crystals that are easily disrupted. Whether the displacements are static or in motion during the exposure does not affect the obtained diffraction, which is an average across the illuminated volume of the crystal and time. Thus, it may be possible to induce angstrom-scale acoustic modes in the crystal to achieve or enhance the continuous diffraction. At resolutions higher than the inverse of the disorder length, one can treat the crystal simply as a convenient way to place many aligned molecules in the X-ray beam, just like a gas of aligned molecules, to obtain the incoherent sum of the aligned-molecule diffraction (Fig. 3). Just as in aligned-molecule diffraction, random rigid-body rotations of the molecules give rise to a blurring of the continuous diffraction intensities that gets worse with increasing scattering angle. To avoid smearing out an individual speckle at the highest resolution, the width of the distribution of the rotations should be $\Delta\phi < d/w$, for a molecule of width w, equivalent to the Crowther condition in tomography [101]. The condition for this incoherent blurring is less stringent than the translations that disrupt the coherent interference at the Bragg peaks. The ultimate resolution of the continuous diffraction, therefore, will depend on the degree of rotational disorder and internal variabilities of the molecules.

The molecules in a crystal are aligned in several discrete orientations following the point group symmetry of the crystal. For example, photosystem II crystals have the space group symmetry $P2_12_12_1$ consisting of four dimers in unique orientations found by rotating any one of them by 180° about each of the three orthogonal axes of the orthorhombic cell (point group 222). Assuming no correlation between the translations and the orientation of molecules, the continuous diffraction is proportional to the incoherent sum of the dimer diffraction in these four orientations. For a spherically shaped molecule this overlap of orientations would reduce the information content of the continuous diffraction by a factor of four; less, if the object is non-spherical, since the summed autocorrelation functions of the various orientations will not completely overlap and hence will be partially distinguishable. In the case of photosystem II, the information content of the continuous diffraction exceeded that required to describe the dimer by a factor of 2.1 (compared with a factor of 0.86 for the Bragg peaks when accounting for the solvent fraction of the crystal) [41].

Periodicity concentrates the diffracting photons into narrow Bragg peaks that can be delineated from the background. The continuous diffraction of a disordered crystal contains as many diffracted photons as in the Bragg peaks of the same resolution from an ordered crystal—the scattering strength of atoms does not

depend on their location or relation to each other. However, the continuous diffraction signal is much lower than that of Bragg peaks since the photons are spread out over many more pixels. For an average spacing of 10 pixels between Bragg peaks, for example, the continuous diffraction signal will be about 1% of that of the ordered crystal. It is also more difficult to separate the continuous diffraction from the continuous background. Its measurement requires the precautions described above to create experimental conditions with the lowest possible background. By perfecting these experiments it should be possible to further extend the achievable resolution, and to use the additional diffraction information to obtain direct information of conformational variability. This will be helped by reducing the crystal size, perhaps down to single molecules.

6 Conclusions

Free electron lasers have enabled some new paradigms for structure determination of macromolecules, and opened up new capabilities for time-resolved imaging and obtaining images from samples too small for conventional X-ray analysis. One of the main methodological innovations to use XFEL pulses, serial crystallography, and diffraction has also been shown to provide benefits when used with synchrotron radiation by being able to gather high-resolution structural information at room temperature without having to expose samples to the limits of their tolerable doses. Serial crystallography can be thought of as powder diffraction, measured one grain at a time, allowing the ensemble to be consolidated in the frame of reference of the lattice, instead of simply summing all patterns in the laboratory frame of the detector. As such, the only requirement from a single pattern is that it gives enough information to place it, in three-dimensional reciprocal space, in relation to other patterns. It has been demonstrated that millions of extremely weak patterns can be treated this way, as long as background scatter is small. Thus, the ingredients for this paradigm are a tightly focused intense X-ray beam of bandwidth up to a few percent; a method to rapidly replenish the sample into the beam that generate the lowest possible background; a high frame-rate integrating pixellated detector to record patterns of individual objects fed through the beam; and software to consolidate all diffraction data in a common frame of reference. At free-electron lasers, conventional dose limits are overcome by using femtosecond-duration pulses, which may enable exposures with such high fluences to give as many elastically scattered photons into the diffraction pattern as there are atoms in the sample, which should be enough to carry out single-molecule diffraction. The number of required patterns decreases sharply with the size of the crystalline

samples, but low background and strong exposures from small crystals have enabled time-resolved measurements over timescales from below 1 ps to several seconds, as well as new phasing methods. In particular, strong exposures and low backgrounds let us measure diffraction beyond the highest scattering angles of visible Bragg peaks to acquire the continuous diffraction from single molecules in a translationally disordered crystal. Serial crystallography requires sources of high average brightness and high peak brightness (or peak power) and schemes to reach peak powers of 1 TW (e.g., giving 10^{12} photons in 1 fs) and repetition rates approaching or even exceeding 1 MHz, will enable dramatic increases in capabilities, surpassing those we have witnessed in the initial experiments at X-ray free electron lasers.

References

1. McNeil BWJ, Thompson NR (2010) X-ray free-electron lasers. Nat Photon 4:814–821
2. Liu W, Wacker D, Gati C et al (2013) Serial femtosecond crystallography of G protein-coupled receptors. Science 342:1521–1524
3. Zhou Q, Lai Y, Bacaj T et al (2015) Architecture of the synaptotagmin-snare machinery for neuronal exocytosis. Nature 525:62–67
4. DePonte DP, Weierstall U, Schmidt K et al (2008) Gas dynamic virtual nozzle for generation of microscopic droplet streams. J Phys D41:195505
5. Weierstall U, Spence JCH, Doak RB (2012) Injector for scattering measurements on fully solvated biospecies. Rev Sci Instrum 83:035108
6. Weierstall U, James D, Wang C et al (2014) Lipidic cubic phase injector facilitates membrane protein serial femtosecond crystallography. Nat Commun 5:3309
7. Sugahara M, Mizohata E, Nango E et al (2015) Grease matrix as a versatile carrier of proteins for serial crystallography. Nat Methods 12:61–63
8. Conrad CE, Basu S, James D et al (2015) A novel inert crystal delivery medium for serial femtosecond crystallography. IUCrJ 2:421–430
9. Bogan M, Benner W, Boutet S et al (2008) Single particle X-ray diffractive imaging. Nano Lett 8:310–316
10. Zarrine-Afsar A, Müller C, Talbot FO et al (2011) Self-localizing stabilizing mega-pixel picoliter arrays with size-excluding sorting capabilities. Anal Chem 83:767–773
11. Hunter MS, Segelke B, Messerschmidt M et al (2014) Fixed-target protein serial microcrystallography with an X-ray free electron laser. Sci Rep 4:6026
12. Roedig P, Vartiainen I, Duman R et al (2015) A micro-patterned silicon chip as sample holder for macromolecular crystallography experiments with minimal background scattering. Sci Rep 5:10451
13. Kirian RA, White TA, Holton JM et al (2011) Structure-factor analysis of femtosecond microdiffraction patterns from protein nanocrystals. Acta Crystallogr A 67:131–140
14. Neutze R, Wouts R, van der Spoel D et al (2000) Potential for biomolecular imaging with femtosecond X-ray pulses. Nature 406:753–757
15. Huldt G, Szoke A, Hajdu J (2003) Diffraction imaging of single particles and biomolecules. J Struct Biol 144:219–227
16. Frank M, Carlson DB, Hunter MS et al (2014) Femtosecond X-ray diffraction from two-dimensional protein crystals. IUCrJ 1:95–100
17. Küpper J, Stern S, Holmegaard L et al (2014) X-ray diffraction from isolated and strongly aligned gas-phase molecules with a free-electron laser. Phys Rev Lett 112:083002
18. Barends TRM, Foucar L, Ardevol A et al (2015) Direct observation of ultrafast collective motions in co myoglobin upon ligand dissociation. Science 350:445–450
19. Pande K, Hutchison CDM, Groenhof G et al (2016) Femtosecond structural dynamics drives the trans/cis isomerization in photoactive yellow protein. Science 352:725–729

20. Schmidt M (2013) Mix and inject: reaction initiation by diffusion for time-resolved macromolecular crystallography. Adv Cond Matter Phys 10:167276
21. Henderson R (1995) The potential and limitations of neutrons, electrons and X-rays for atomic resolution microscopy of unstained biological molecules. Q Rev Biophys 28:171–193
22. Chapman HN, Caleman C, Timneanu N (2014) Diffraction before destruction. Philos Trans R Soc B369:20130313
23. Creagh DC, Hubbell JH (2006) X-ray absorption (or attenuation) coefficients. Int Tables Crystallogr C:220–229
24. Son S-K, Young L, Santra R (2011) Impact of hollow-atom formation on coherent X-ray scattering at high intensity. Phys Rev A83:033402
25. Caleman C, Ortiz C, Marklund E et al (2009) Radiation damage in biological material: electronic properties and electron impact ionization in urea. Europhys Lett 85:18005, erratum 88: 29901
26. Barty A, Caleman C, Aquila A et al (2012) Self-terminating diffraction gates femtosecond X-ray nanocrystallography measurements. Nat Photon 6:35–40
27. Nass K, Foucar L, Barends TRM et al (2015) Indications of radiation damage in ferredoxin microcrystals using high-intensity X-FEL beams. J Synchrotron Radiat 22:225–238
28. Son S-K, Chapman HN, Santra R (2011) Multiwavelength anomalous diffraction at high X-ray intensity. Phys Rev Lett 107:218102
29. Son S-K, Chapman HN, Santra R (2013) Determination of multiwavelength anomalous diffraction coefficients at high X-ray intensity. J Phys B46:164015
30. Galli L, Son S-K, Barends TRM et al (2015) Towards phasing using high X-ray intensity. IUCrJ 2:627–634
31. Serkez S, Kocharyan V, Saldin E et al (2013) Proposal for a scheme to generate 10 TW-level femtosecond X-ray pulses for imaging single protein molecules at the European XFEL. arXiv.org:1306.0804
32. Davis KM, Kosheleva I, Henning RW et al (2013) Kinetic modeling of the X-ray-induced damage to a metalloprotein. J Phys Chem B117:9161–9169
33. Owen RL, Rudino-Pinera E, Garman EF (2006) Experimental determination of the radiation dose limit for cryocooled protein crystals. Proc Natl Acad Sci U S A 103:4912–4917
34. Garman EF, Weik M (2015) Radiation damage to macromolecules: kill or cure? J Synchrotron Radiat 22:195–200
35. Cowan A, Nave C (2008) The optimum conditions to collect X-ray data from very small samples. J Synchrotron Radiat 15:458–462
36. Coquelle N, Brewster AS, Kapp U et al (2015) Raster-scanning serial protein crystallography using micro- and nano-focused synchrotron beams. Acta Crystallogr D Biol Crystallogr 71:1184–1196
37. Koopmann R, Cupelli K, Redecke L et al (2012) In vivo protein crystallization opens new routes in structural biology. Nat Methods 9:259–262
38. Redecke L, Nass K, DePonte DP et al (2013) Natively inhibited Trypanosoma brucei cathepsin B structure determined by using an X-ray laser. Science 339:227–230
39. Jakobi AJ, Passon DM, Knoops K et al (2016) In cellulo serial crystallography of alcohol oxidase crystals inside yeast cells. IUCrJ 3: 88–95
40. Sawaya MR, Cascio D, Gingery M et al (2014) Protein crystal structure obtained at 2.9 Å resolution from injecting bacterial cells into an X-ray free-electron laser beam. Proc Natl Acad Sci U S A 111:12769–12774
41. Ayyer K, Philipp HT, Tate MW et al (2015) Determination of crystallographic intensities from sparse data. IUCrJ 2:29–34
42. Wierman JL, Lan T-Y, Tate MW et al (2016) Protein crystal structure from non-oriented, single-axis sparse X-ray data. IUCrJ 3: 43–50
43. Loh NTD, Elser V (2009) Reconstruction algorithm for single-particle diffraction imaging experiments. Phys Rev E80:026705
44. Fung R, Shneerson V, Saldin DK et al (2009) Structure from fleeting illumination of faint spinning objects in flight. Nat Phys 5:64–67
45. White TA (2014) Post-refinement method for snapshot serial crystallography. Philos Trans R Soc B369:20130330
46. Gati C, Oberthuer D, Yefanov O et al (2017) Atomic structure of granulin determined from native nanocrystalline granulovirus using an X-ray free-electron laser. Proc Natl Acad Sci U S A 114:2247–2252
47. Galli L, Metcalf P, Chapman HN (2015) Implications of the focal beam profile in serial femtosecond crystallography. Proc SPIE 9511:95110H
48. Liang M, Williams GJ, Messerschmidt M et al (2015) The coherent X-ray imaging instrument at the linac coherent light source. J Synchrotron Radiat 22:514–519

49. Hart P, Boutet S, Carini G et al (2012) The CSPAD megapixel X-ray camera at LCLS. Proc SPIE 8504:85040C–850411
50. Kärtner F, Ahr F, Calendron A-L et al (2016) AXSIS: exploring the frontiers in attosecond X-ray science, imaging and spectroscopy. Nucl Instrum Methods Phys Res A829:24–29
51. Allahgholi A, Becker J, Bianco L et al (2015) AGIPD, a high dynamic range fast detector for the European XFEL. J Instrum 10:C01023
52. Brehm W, Diederichs K (2014) Breaking the indexing ambiguity in serial crystallography. Acta Crystallogr D Biol Crystallogr 70:101–109
53. Ginn HM, Messerschmidt M, Ji X et al (2015) Structure of CPV17 polyhedrin determined by the improved analysis of serial femtosecond crystallographic data. Nat Commun 6:6435
54. Barends TRM, Foucar L, Botha S et al (2014) *De novo* protein crystal structure determination from X-ray free-electron laser data. Nature 505:244–247
55. Nakane T, Song C, Suzuki M (2015) Native sulfur/chlorine SAD phasing for serial femtosecond crystallography. Acta Crystallogr D Biol Crystallogr 71:2519–2525
56. Nass K, Meinhart A, Barends TRM et al (2016) Protein structure determination by single-wavelength anomalous diffraction phasing of X-ray free-electron laser data. IUCrJ 3:180–191
57. Schmidt S (2014) GrainSpotter: a fast and robust polycrystalline indexing algorithm. J Appl Crystallogr 47:276–284
58. Gildea RJ, Waterman DG, Parkhurst JM et al (2014) New methods for indexing multi-lattice diffraction data. Acta Crystallogr D Biol Crystallogr 70:2652–2666
59. Ginn HM, Roedig P, Kuo A et al (2016) TakeTwo: an indexing algorithm suited to still images with known crystal parameters. Acta Crystallogr D Biol Crystallogr 72:956–965
60. White TA, Barty A, Stellato F et al (2013) Crystallographic data processing for free-electron laser sources. Acta Crystallogr D Biol Crystallogr 69:1231–1240
61. Hirata K, Shinzawa-Itoh K, Yano N et al (2014) Determination of damage-free crystal structure of an X-ray-sensitive protein using an XFEL. Nat Methods 11:734–736
62. Cohen AE, Soltis SM, Gonzalez A et al (2014) Goniometer-based femtosecond crystallography with X-ray free electron lasers. Proc Natl Acad Sci U S A 111:17122–17127
63. Diederichs K, Karplus PA (2013) Better models by discarding data? Acta Crystallogr D Biol Crystallogr 69:1215–1222
64. Zhang T, Jin S, Gu Y et al (2015) SFX analysis of non-biological polycrystalline samples. IUCrJ 2:322–326
65. Liu Q, Dahmane T, Zhang Z et al (2012) Structures from anomalous diffraction of native biological macromolecules. Science 336:1033–1037
66. Schlichting I (2015) Serial femtosecond crystallography: the first five years. IUCrJ 2:246–255
67. Chavas LMG, Gumprecht L, Chapman HN (2015) Possibilities for serial femtosecond crystallography sample delivery at future light sources. Struct Dyn 2:041709
68. Chapman HN (2015) Serial femtosecond crystallography. Synchrotron Radiat News 28:20–24
69. Gruner SM, Lattman EE (2015) Biostructural science inspired by next-generation X-ray sources. Annu Rev Biophys 44:33–51
70. Boutet S, Williams SG (2010) The coherent X-ray imaging (CXI) instrument at the linac coherent light source (LCLS). New J Phys 12:035024
71. Bozek JD (2009) AMO instrumentation for the LCLS X-ray FEL. Eur Phys J 169:129–132
72. Song C, Tono K, Park J et al (2014) Multiple application X-ray imaging chamber for single-shot diffraction experiments with femtosecond X-ray laser pulses. J Appl Crystallogr 47:188–197
73. Chapman HN, Fromme P, Barty A et al (2011) Femtosecond X-ray protein nanocrystallography. Nature 470:73–77
74. Gañan Calvo AM (1998) Generation of steady liquid microthreads and micron-sized monodisperse sprays in gas streams. Phys Rev Lett 80:285–288
75. Awel S, Kirian RA, Eckerskorn N et al (2016) Visualizing aerosol-particle injection for diffractive-imaging experiments. Opt Express 24:6507–6521
76. Stan CA, Milathianaki D, Laksmono H et al (2016) Liquid explosions induced by X-ray laser pulses. Nat Phys 12:966–971
77. Roessler CG, Kuczewski A, Stearns R et al (2013) Acoustic methods for high-throughput protein crystal mounting at next-generation macromolecular crystallographic beamlines. J Synchrotron Radiat 20:805–808
78. Ganan-Calvo AM, Gonzalez-Prieto R, Riesco-Chueca P (2007) Focusing capillary jets close to the continuum limit. Nat Phys 3:737–742
79. Wang D, Weierstall U, Pollack L et al (2014) Double-focusing mixing jet for XFEL study

of chemical kinetics. J Synchrotron Radiat 21:1364–1366
80. Oberhuer D et al (2017) Room-temperature structure determination of RNA polymerase II enabled by double-flow focusing injection. Sci Rep 7:44628
81. Lee C-Y, Chang C-L, Wang Y-N et al (2011) Microfluidic mixing: a review. Int J Mol Sci 12:3263
82. Liu P, Ziemann PJ, Kittleson DB et al (1995) Generating particle beams of controlled dimensions and divergence: I. Theory of particle motion in aerodynamic lenses and nozzle expansions. Aerosol Sci Technol 22:314–324
83. Seibert MM, Ekeberg T, Maia FRNC et al (2011) Single mimivirus particles intercepted and imaged with an X-ray laser. Nature 470:78–81
84. Aquila A, Barty A, Bostedt C et al (2015) The linac coherent light source single particle imaging road map. Struct Dyn 2:041701
85. Eckerskorn N, Bowman R, Kirian RA et al (2015) Optically induced forces imposed in an optical funnel on a stream of particles in air or vacuum. Phys Rev Appl 4:064001
86. Sherrell DA, Foster AJ, Hudson L et al (2015) A modular and compact portable mini-endstation for high-precision, high-speed fixed target serial crystallography at FEL and synchrotron sources. J Synchrotron Radiat 22:1372–1378
87. Yuk JM, Park J, Ercius P et al (2012) High-resolution EM of colloidal nanocrystal growth using graphene liquid cells. Science 336:61–64
88. Spence JCH, Kirian RA, Wang X et al (2011) Phasing of coherent femtosecond X-ray diffraction from size- varying nanocrystals. Opt Express 19:2866–2873
89. Kirian RA, Bean RJ, Beyerlein KR et al (2015) Direct phasing of finite crystals illuminated with a free-electron laser. Phys Rev X 5:011015
90. Ayyer K, Yefanov OM, Oberthür D (2016) Macromolecular diffractive imaging using imperfect crystals. Nature 530:202–206
91. Millane RP (1990) Phase retrieval in crystallography and optics. J Opt Soc Am A 7:394–411
92. Sayre D, Chapman HN (1995) X-ray microscopy. Acta Crystallogr A 51:237–252
93. Sayre D (1952) Some implications of a theorem due to Shannon. Acta Crystallogr 5:843
94. Oszlányi G, Süto A (2008) The charge flipping algorithm. Acta Crystallogr A 64:123–134
95. Elser V, Millane RP (2008) Reconstruction of an object from its symmetry-averaged diffraction pattern. Acta Crystallogr A 64:273–279
96. Thibault P, Elser V (2010) X-ray diffraction microscopy. Annu Rev Cond Matter Phys 1:237–255
97. Fienup JR (1982) Phase retrieval algorithms: a comparison. Appl Opt 21:2758–2769
98. Bragg L, Perutz MF (1952) The structure of Haemoglobin. Proc R Soc Lond 213:425–435
99. He H, Su W-P (2015) Direct phasing of protein crystals with high solvent content. Acta Crystallogr A 71:92–98
100. Wall ME, Adams PD, Fraser JS et al (2014) Diffuse X-ray scattering to model protein motions. Structure 22:182–184
101. Crowther R, DeRosier D, Klug A (1970) The reconstruction of a three-dimensional structure from its projections and its applications to electron microscopy. Proc R Soc Lond 317:319–340
102. Roedig P, Duman R, Sanchez-Weatherby J et al (2016) Room-temperature macromolecular crystallography using a micro-patterned silicon chip with minimal background scattering. J Appl Crystallogr 49:968–975
103. Stellato F, Oberthür D, Liang M et al (2014) Room-temperature macromolecular serial crystallography using synchrotron radiation. IUCrJ 1:204–212
104. Nogly P, James D, Wang D et al (2015) Lipidic cubic phase serial millisecond crystallography using synchrotron radiation. IUCrJ 2:168–176
105. Botha S, Nass K, Barends TRM et al (2015) Room-temperature serial crystallography at synchrotron X-ray sources using slowly flowing free-standing high-viscosity microstreams. Acta Crystallogr D Biol Crystallogr 71:387–397
106. Boutet S, Lomb L, Williams GJ et al (2012) High-resolution protein structure determination by serial femtosecond crystallography. Science 337:362–364
107. Gati C, Bourenkov G, Klinge M et al (2014) Serial crystallography on in vivo grown microcrystals using synchrotron radiation. IUCrJ 1:87–94
108. Kupitz C, Basu S, Grotjohann I et al (2014) Serial time-resolved crystallography of photosystem II using a femtosecond X-ray laser. Nature 513:261–265
109. Pedrini B, Tsai C-J, Capitani G et al (2014) 7 Å resolution in protein two-dimensional-crystal X-ray diffraction at linac coherent light source. Philos Trans R Soc Lond B Biol Sci B369:20130500
110. Holton JM (2009) A beginner's guide to radiation damage. J Synchrotron Radiat 16:133–142